



Research paper

Design and facile one-step synthesis of FeWO₄/Fe₂O₃ di-modified WO₃ with super high photocatalytic activity toward degradation of quasi-phenothiazine dyes



Huixiang Wang^{a,c}, Conghui Wang^{a,c}, Xinmin Cui^{a,c}, Li Qin^{a,c}, Ruimin Ding^a, Liancheng Wang^a, Zhong Liu^b, Zhanfeng Zheng^a, Baoliang Lv^{a,*}

^a State Key Laboratory of Coal Conversion, Institute of Coal Chemistry, Chinese Academy of Sciences, Taiyuan, 030001, China

^b Key Laboratory of Salt Lake Resources and Chemistry, Qinghai Institute of Salt Lakes, Chinese Academy of Sciences, Xining, 810008, China

^c University of Chinese Academy of Sciences, Beijing, 100049, China

ARTICLE INFO

Keywords:

Modified WO₃
Photodegradation
Quasi-phenothiazine dyes
Fenton reaction

ABSTRACT

For most of WO₃, a visible-light-driven photocatalyst, its barrier in photocatalytic degradation is the low conduction band (CB) potential that can not reduce O₂ to O₂^{•-} and HO₂[•] radicals and thus results in fast recombination of electron/hole. With this in mind, a new active FeWO₄/Fe₂O₃ di-modified WO₃ was designed and prepared via a straightforward but effective strategy by introducing of FeWO₄ and Fe₂O₃ clusters (or nanoparticles) on WO₃. The performance of di-modified WO₃ showed super high photocatalytic activity in degrading quasi-phenothiazine dyes of Methylene blue (MB), Toluidine blue (TB), Azure I (AI) and Acridine orange (AO) under visible light irradiation, and the corresponding *k* values are 5.3, 4.4, 3.8 and 5.8 times larger than that of pure WO₃, respectively. This improvement was mainly due to the fact that photoexcited electrons can migrate to the matching CB of firmly and highly dispersed FeWO₄ and Fe₂O₃, then be consumed rapidly by a valence decrease from Fe³⁺ to Fe²⁺ and Fenton reaction between Fe²⁺ and H₂O₂. And the strong adsorption of Fe species toward N and S (or N) elements in quasi-phenothiazine dyes, also positively promoted the efficiency of degradation.

1. Introduction

During the last decades, semiconductor photocatalytic materials applied to degradation of organic pollutants in water and air have attracted much attention with a view to obtaining clean environment and utilizing renewable energy [1–3]. In the process of effective photodegradation, two main problems must be resolved, i.e. (1) improving the quantum efficiency which means decreasing the recombination of photoexcited electron/hole; (2) extending the excitation wavelength range of photocatalysts which means making full use of visible light. To achieve above goals, design and preparation of suitable semiconductor photocatalysts are the core tasks.

Tungsten oxide (WO₃) as one of the most promising photocatalysts has a small band gap *E*_g (2.4–2.8 eV) that makes it possible to carry out photocatalytic degradation of organic contaminants under visible light. However, for most of WO₃ materials, they are rarely used in photodegradation, because the lower conduction band (CB) edge (+0.2 to +0.8 V_{NHE}) [4,5] of WO₃ does not provide a sufficient potential for single-electron reduction of O₂ [*E*⁰(O₂/O₂^{•-}) = −0.33 V_{NHE} and

*E*⁰(O₂/HO₂[•]) = −0.05 V_{NHE}] [6,7], even though the higher valence band (VB) can oxidize H₂O to a large amount of O₂ [*E*⁰(O₂/H₂O) = 1.23 V_{NHE}] [8] and some •OH [*E*⁰(•OH/H₂O) = 2.38 V_{NHE}] [9]. Consequently, the photoexcited electrons are not effectively separated and utilized by O₂, and this inevitably results in recombination of electron/hole and low quantum efficiency of pure WO₃. To overcome this shortcoming, hydrogen peroxide (H₂O₂) can be directly introduced into the photocatalytic system as electron acceptor to produce some •OH radicals, but its activity is very limited [9,10]. In addition, deposition of noble metal such as Pt and Ag on WO₃ surface can result in multielectron reduction of O₂, but the limited reserve suppresses its extensive application [11–13]. Besides, the photocatalytic activity of WO₃ could be significantly improved by combining with other metal oxides (MO), including CuO and Fe₂O₃ etc. [7,14,15], because these MO could act as electron sink to capture the photoinduced electrons through its low energy trapping sites [16] and then consume them by a valence decrease of MO (Cu²⁺→Cu⁺, Fe³⁺→Fe²⁺) due to their stronger oxidizing ability than O₂. In short, the electron consumption could reduce the electron/hole recombination and enhance the efficiency of the

* Corresponding author at: State Key Laboratory of Coal Conversion, Institute of Coal Chemistry, Chinese Academy of Sciences, Taiyuan, 030001, China.
E-mail address: lb604@sxicc.ac.cn (B. Lv).

<http://dx.doi.org/10.1016/j.apcatb.2017.09.011>

Received 20 January 2017; Received in revised form 6 April 2017; Accepted 4 September 2017

Available online 09 September 2017

0926-3373/ © 2017 Elsevier B.V. All rights reserved.

charge separation. In contrast, this method shows great advantages in making efficient and economic photocatalysts.

Among numerous MO materials, the Fe_2O_3 is also a visible-light-driven material with the E_g of 2.0–2.3 eV [17] and the CB of 0.46–0.77 eV [14], hence just as the WO_3 , it shows poor activity in degradation of organic pollutants. However, in the presence of trace H_2O_2 , the classical Fenton reaction can effectively make full use of the photoinduced electrons, finally improving the quantum efficiency and photocatalytic activity. Based on this promising process, the Fe_2O_3 becomes an ideal candidate to be composed with WO_3 because the CB of two materials is matchable in energy. Of course, we ought to broaden our horizon and find a semiconductor with similar E_g structure to the Fe_2O_3 to jointly modify the WO_3 and hasten the electron migration and separation. Then the FeWO_4 emerges as the best candidate due to appropriate E_g (1.78–2.35 eV) and CB (0.55–0.73 eV) [18–21] which are equal to Fe_2O_3 and WO_3 . So it can be predicted that such a $\text{FeWO}_4/\text{Fe}_2\text{O}_3$ di-modified WO_3 might exhibit higher activity in photo-degradation reaction in the presence of trace H_2O_2 .

In this paper, we successfully prepared the $\text{FeWO}_4/\text{Fe}_2\text{O}_3$ di-modified WO_3 photocatalysts by introducing the FeWO_4 and Fe_2O_3 clusters (or nanoparticles) on WO_3 surface via a facile one-step method. Comparing with the pure WO_3 , the obtained $\text{FeWO}_4/\text{Fe}_2\text{O}_3$ di-modified WO_3 materials showed super high activity in photocatalytic degradation of quasi-phenothiazine dyes under visible light ($\lambda > 420$ nm) when trace H_2O_2 was used as electron capture agent. This work perfectly combined such three cheap materials of WO_3 , FeWO_4 and Fe_2O_3 together and effectively degraded organic pollutants under visible light, so it well meets the requirements of today's environmental protecting, energy saving and efficient economy.

2. Experimental section

2.1. Materials and methods

2.1.1. Materials

All chemicals were used without further purification. Ferric nitrate ($\text{Fe}(\text{NO}_3)_3 \cdot 9\text{H}_2\text{O}$, 99.0%) was purchased from China Medicament Co. Sodium tungstate ($\text{Na}_2\text{WO}_4 \cdot 2\text{H}_2\text{O}$, 99.5%) and hydrochloric acid (HCl, 36.0–38.0%) were purchased from Tianjin Chemical Reagent Co. Double-distilled water was used throughout the experiment.

2.1.2. Synthesis

In a typical procedure, firstly, 0.23 mmol $\text{Fe}(\text{NO}_3)_3 \cdot 9\text{H}_2\text{O}$ was dissolved in 30 mL distilled water under ultrasonic, and the solution was referred as A. Solution B was 80 mL aqueous with 2.3 mmol $\text{Na}_2\text{WO}_4 \cdot 2\text{H}_2\text{O}$. Secondly, solution A was slowly added to solution B under stirring to form a yellow solution. After that, the pH of above solution was adjusted to 2.0 using 3 M HCl after stirring for an hour, then transferred to a 150 mL autoclave, sealed and maintained at 220 °C for 24 h. After naturally cooled to room temperature, the precipitates were filtered, washed sequentially with water and ethanol to remove remnant ions in the final products, and dried at 60 °C, which was denoted as WFe0.10 . The rest samples with different iron content were synthesized via the similar procedure, and the materials were denoted as $\text{WFe}x$, where x was the mole ratio of Fe/W .

2.2. Catalyst characterization

The crystal phases of products were determined by X-ray powder diffraction (XRD) using a D8 Advance Bruker AXS diffractometer and $\text{Cu-K}\alpha$ radiation ($\lambda = 1.5406$ Å, 40 kV, 100 mA), employing a scan step of 0.01° in the 2θ range of 10 – 70° . The morphologies, element distributions and sizes of samples were observed by scanning electron microscopy (SEM, JSM-7001F) and transmission electron microscopy (TEM, JEOL-2010). The fine crystal structures of the particles were investigated by high-resolution transmission electron microscope

(HRTEM, JEOL-2010). Fourier transform infrared (FT-IR) spectra were obtained by using a Nicolet iS50 FT-IR spectrometer in the range 400 – 4000 cm^{-1} and the specific surface areas of samples were evaluated using the Brunauer-Emmett-Teller method (BET, Micromeritics ASAP3000). The elemental composition and surface chemical state were determined with an X-ray photoelectron spectroscopy (XPS, Mg $\text{K}\alpha$ as radiation source, PHI-5300X, Perkin-Elmer). The actual content of Fe (wt.%) was detected by inductively coupled plasma-atomic emission spectrometry (ICP-AES, Thermo iCAP6300) and photoluminescence spectrum (PL) was obtained with Fluorescence spectrophotometer at working voltage of 400 V and the excitation wavelength was 300 nm (F-7000, Xenon lamp as excitation light source). The UV–vis diffuse reflectance spectrum (DRS) and UV–vis absorption spectrum of solution were obtained with UV–vis spectrophotometer (UV-3150, BaSO_4 as a reference for DRS).

2.3. Photocatalytic experiment

The photocatalytic activities of all prepared $\text{WFe}x$ samples in degradation of organic dyes (Methylene blue (MB), Rhodamine B (RhB), Toluidine blue (TB), Azure I (AI) and Acridine orange (AO)) were performed at a quartz reactor with the cross-sectional area of 28 cm^2 and maintained at 10 °C with cooling water recirculation system. The light source was 300 W Xenon lamp with a 420 nm cut-off filter and the distance between the liquid level and the light source was 15 cm. In a typical process: 10 mg catalyst was dispersed in 50 mL aqueous solution containing organic dye (6 mg L^{-1}) for 5 min with ultrasonic treatment. Next, the suspension was magnetically stirred in the dark for 30 min to reach a complete adsorption-desorption equilibrium. Prior to the irradiation, 3.0 mL suspension was drawn, which was centrifuged to remove the catalyst and the concentration of clear supernatant was marked as C_0 , then 0.97 mmol H_2O_2 (30 wt.%) was introduced to the system. During the following irradiation, analytical sample with 3.0 mL was drawn from the reaction suspension every certain interval time, then centrifuged and analyzed. The concentrations of MB, RhB, TB, AI and AO solutions were determined by recording the variations of maximum absorption band (MB at 664 nm, RhB at 554 nm, TB at 634 nm, AI at 650 nm and AO at 490 nm) using a UV–vis spectrometry. The photocatalytic degradation efficiency (η) of organic dyes was obtained by the following formula:

$$\eta = (1 - C/C_0) \times 100\% = (1 - A/A_0) \times 100\%$$

where, C is the concentration of dyes solution at the reaction time t , C_0 is the adsorption-desorption equilibrium concentration of organic dyes (at reaction time 0); A and A_0 are the corresponding absorbance values.

3. Results and discussion

3.1. Catalysts characterization

The X-ray diffraction (XRD) patterns of unmodified WFe0 (pure WO_3) and di-modified $\text{WFe}x$ ($x = 0.07, 0.10$ and 0.20) are shown in Fig. 1. The WFe0 is typical hexagonal structure of WO_3 (JCPDS 33-1387), perhaps also contains a certain amount of $\text{h-WO}_3 \cdot 0.33\text{H}_2\text{O}$ (JCPDS 35-1001) for the two phases have similar diffraction peaks. The intensity of (001) plane of WFe0 is stronger than that of the standard data, suggesting the preferential orientation along [001] direction [22]. When the Fe^{3+} cations are introduced, new peaks at 18.1° , 23.0° and 27.1° appear in WFe0.07 and can be indexed to (111), (002) and (131) planes of the orthorhombic phase $\text{WO}_3 \cdot 0.33\text{H}_2\text{O}$ (JCPDS 35-0270), and they gradually disappear with increasing the ratio of Fe/W . Thus it can be seen that the Fe^{3+} cations could affect the crystal structure of WO_3 , since Fe^{3+} cations might get into the lattice of WO_3 due to their similar ionic radius (Fe^{3+} : 64 Å, W^{6+} : 62 Å). Notably, no crystalline phase of FeWO_4 or Fe_xO_y is detected until the ratio of Fe/W increases to 0.10,

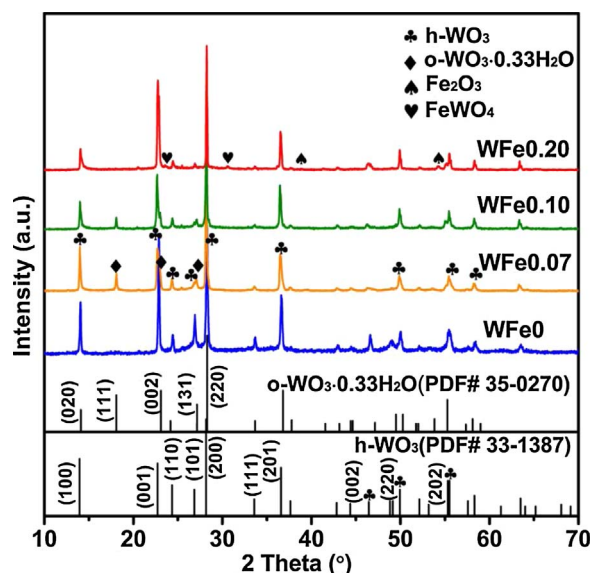


Fig. 1. The XRD of all WFe_x samples and the corresponding diffraction patterns of hexagonal phase WO₃ (33-1387) and orthorhombic phase WO₃·0.33H₂O (35-0270).

probably due to its low concentration (The ICP of Fe content is presented in Table 1: 0.24 wt.% for WFe0.07 and 0.41 wt.% for WFe0.10) or small size (clusters) of both Fe species. However, the weak peaks of FeWO₄ and Fe₂O₃ appear in the WFe0.20 (Fig. S1) with the 1.52 wt.% Fe and this implies small nanoparticles of Fe species might be formed in WFe0.20.

Fourier transform infrared spectroscopy (FTIR) was used to verify the chemical structure of obtained WFe_x samples and the spectra are presented in Fig. 2. For all products, the absorption at 1625 cm⁻¹ (1637 cm⁻¹ for WFe0) corresponds to bending vibration of –OH from adsorbed water respectively, and the peaks at 1600 cm⁻¹ and 1400 cm⁻¹ can be ascribed to the vibration mode of –OH from structural water [23]. For WFe0 sample, the weak peak at 999 cm⁻¹ can be attributed to stretching vibration of terminal W=O [24], suggesting that the WFe0 contains a little structural water and it can be attributed to h-WO₃·0.33H₂O existed in h-WO₃. In addition, the strong peak at 833 cm⁻¹ and the absorption between 786 cm⁻¹ and 480 cm⁻¹ correspond to the stretching vibration of O–W–O. However, above bands have some obvious variations after the introduction of Fe³⁺ cations. For WFe0.07 sample, the vibration of W = O is equal to pure WFe0, but new peak at 876 cm⁻¹ appears which is attributed to the stretching vibration of Fe–O–W [25], and it respectively shifts to 896 cm⁻¹ and 909 cm⁻¹ for WFe0.10 and WFe0.20 with the increasing Fe content due to massive formation of Fe–O–W and stronger interaction between Fe element and WO₃. Simultaneously, the W=O peak of WFe0.10 and WFe0.20 shifts toward lower frequency (973 cm⁻¹) obviously because

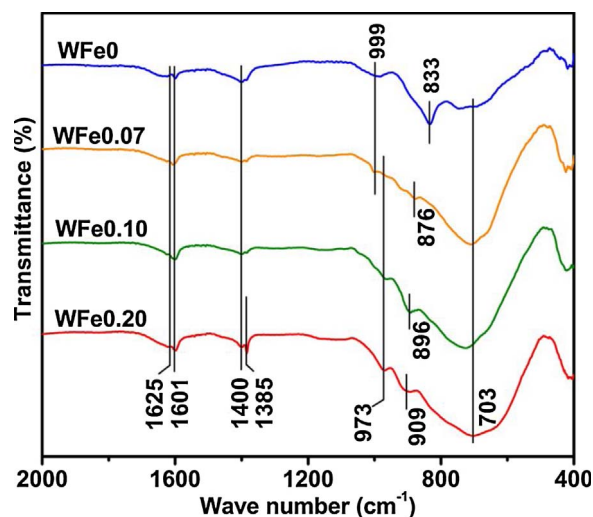


Fig. 2. FTIR spectra of all WFe_x samples: WFe0, WFe0.07, WFe0.10 and WFe0.20.

the Mulliken electronegativity of W and O are stronger of Fe (4.41, 7.54 and 4.06 eV for W, O and Fe, respectively), and this makes the electrons of Fe shift to the W=O band and thus leads to a red shift of W=O. The vibrations of O–Fe–O and O–W–O are almost at same position, which causes the big absorption band between 871 cm⁻¹ and 480 cm⁻¹ for all di-modified WFe_x samples [26,27]. Moreover, the distinct peak at 1385 cm⁻¹ of WFe0.20 can be from the vibration of residual NO₃⁻ anions owing to the larger adsorption capacity of WFe0.20.

The scanning electron microscopy (SEM) images of WFe_x samples (Fig. 3) show that the Fe³⁺ cations have a significant effect on changing the morphology of synthesized products. Without Fe³⁺ cations, the pure WFe0 (Fig. 3a) consisted of nanorods with mean diameter of 250 nm and length to several micrometers. When few Fe³⁺ cations are added to the system, the morphology of nanorods sharply changes to irregular hexagonal sheets of WFe0.07 (Fig. 3b). With continuously increasing Fe content, the irregular hexagonal sheets turn to regular hexagonal prisms and the diameter and thickness become uniform (500–800 nm and 300–500 nm, respectively.) in WFe0.10 (Fig. 3c). For WFe0.20, it can be seen that a great number of agglomerated nanoparticles appear on the surface of hexagonal prisms (Fig. 3d) because of rapid partial precipitation of WO₃ and formation of FeWO₄ and Fe₂O₃ nanoparticles in the preparation process, and these irregular nanoparticles are identified as the mixture of FeWO₄, Fe₂O₃ and WO₃ by HRTEM and corresponding EDX mapping images (Fig. S2 & S3). And the structure diagrammatic sketch of three materials is showed in Fig. 3e. The specific surface areas (BET) of all WFe_x are presented in Table 1. Obviously, the initial introduction of Fe³⁺ cations leads to descent in BET mainly because of the sharp change in morphology. However, the specific surface areas increase gradually with Fe content

Table 1

The properties of different catalysts and their photodegradation apparent rate constant *k* values.

Sample	BET (m ² g ⁻¹)	Fe species (wt.%)		<i>E_g</i> (eV)	<i>k</i> (min ⁻¹)		<i>k_s</i> (MB) (min ⁻¹ m ⁻² g)
		FeWO ₄	Fe ₂ O ₃		MB	RhB	
WFe0	18.66	–	–	2.79	5.62 × 10 ⁻²	2.89 × 10 ⁻²	0.30 × 10 ⁻²
WFe0.07	1.10	5.47	0.81	2.68	5.52 × 10 ⁻²	0.75 × 10 ⁻²	5.00 × 10 ⁻²
WFe0.10	4.81	7.96	1.18	2.62	17.47 × 10 ⁻²	0.91 × 10 ⁻²	3.64 × 10 ⁻²
WFe0.20	13.51	14.56	2.16	2.31	29.87 × 10 ⁻²	1.11 × 10 ⁻²	2.21 × 10 ⁻²
α-Fe ₂ O ₃	12.03	0	100	2.0–2.3 ^a	0.40 × 10 ⁻²	–	0.033 × 10 ⁻²
FeWO ₄	3.06	100	0	1.78–2.35 ^a	1.50 × 10 ⁻²	–	0.490 × 10 ⁻²
c-WO ₃	40.77	–	–	2.4–2.8 ^a	0.96 × 10 ⁻²	–	0.024 × 10 ⁻²
P25	48.90	–	–	~3.20 ^a	1.53 × 10 ⁻²	–	0.031 × 10 ⁻²

Photodegradation conditions: 10 mg catalyst; 50 mL aqueous solution containing organic dyes (6 mg L⁻¹); λ > 420 nm a: the data come from relevant literatures. The content of Fe species was calculated according to the experimental data and the ratio of Fe²⁺ and Fe³⁺ in XPS spectrum.

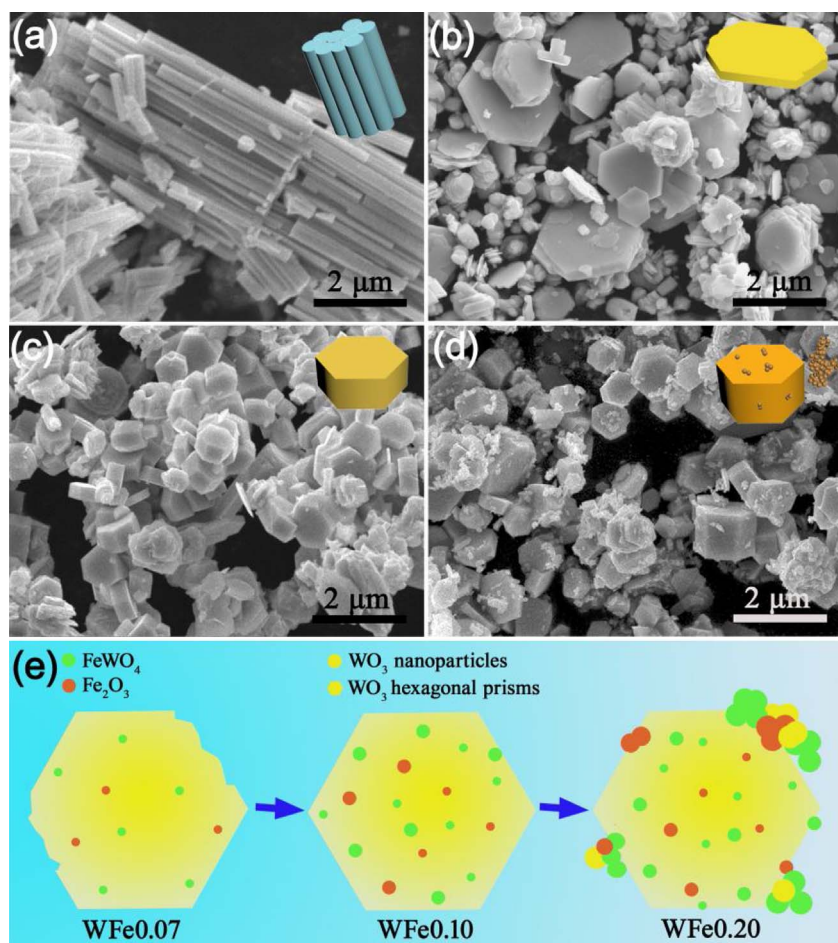


Fig. 3. The SEM morphologies of all WFe: (a) WFe0, (b) WFe0.07, (c) WFe0.10, (d) WFe0.20 and (e) the structure diagrammatic sketch of three samples.

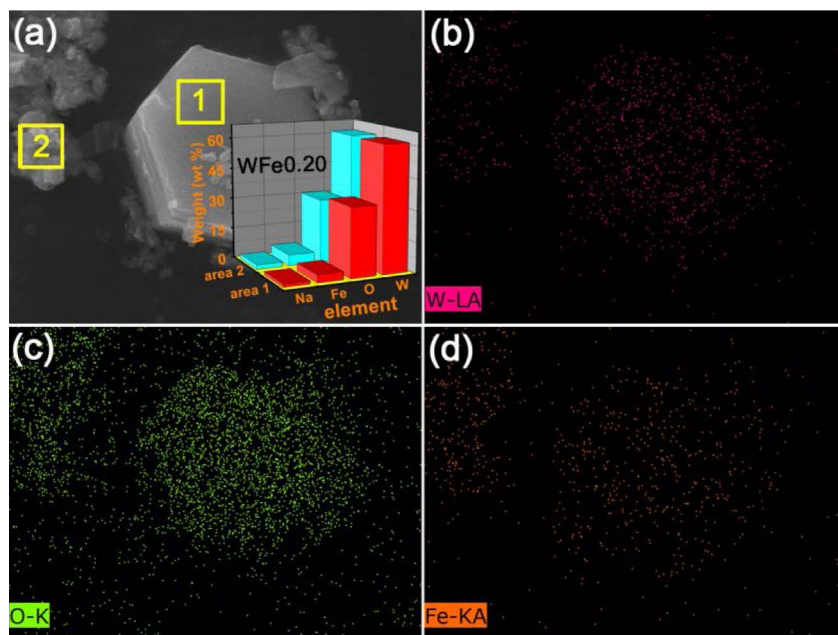


Fig. 4. The mapping of WFe0.20 sample and the element content (wt. %) in different regions.

and there is a sharp increase in WFe0.20, of which the specific surface area is $13.51 \text{ m}^2 \text{ g}^{-1}$. This is because agglomerated nanoparticles contribute to the specific surfaces area, and they also rapidly increase the Fe content (Fe 1.52 wt.%) of WFe0.20. The elemental mapping with proof function is showed in Fig. 4, strongly suggesting that the Fe content in these nanoparticles is higher than that in hexagonal prism

because FeWO₄ and Fe₂O₃ nanoparticles mainly exist in these agglomerated particles while their clusters disperse on the surface of hexagonal prism (Fig. S3), and Fe element in both morphologies is uniformly distributed and there are no large individual particles of FeWO₄ and Fe₂O₃, so they are considered to be smaller nanoparticles and dispersed homogeneously on surface of WO₃.

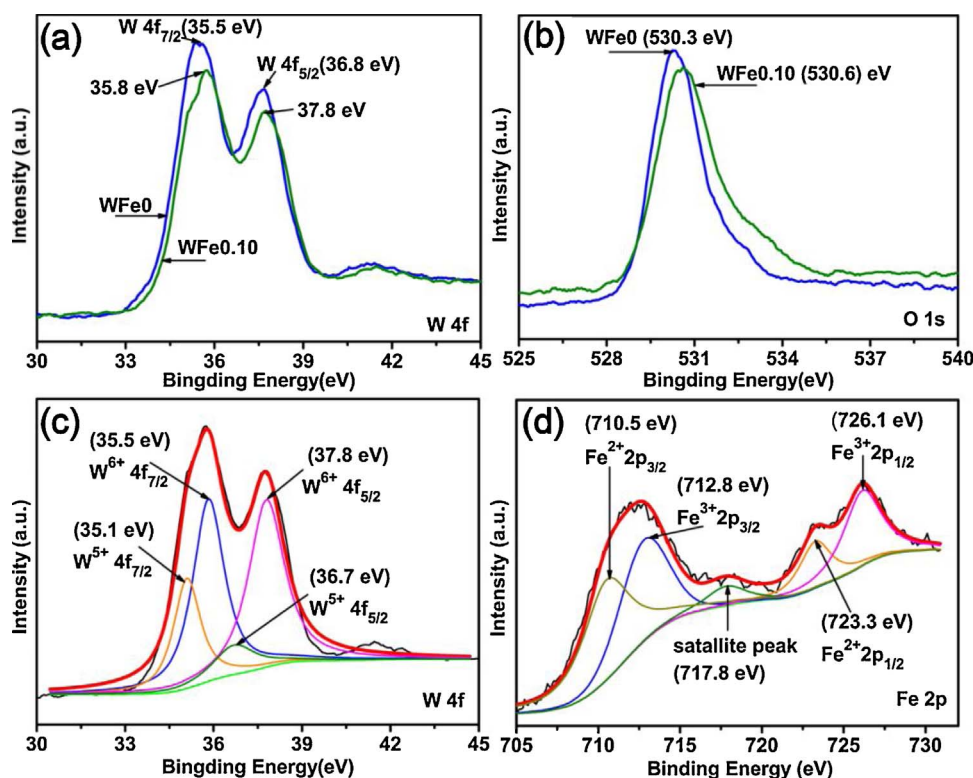


Fig. 5. The XPS spectra of the as-synthesized samples: (a,b) W 4f and O 1s binding energy spectra for both WFe0.10 and WFe0, and (c,d) W 4f and Fe 2p for WFe0.10.

The high-resolution X-ray photoelectron spectra (XPS) of W and O in WFe0 and WFe0.10 are shown in Fig. 5a & b. The peaks at 35.5 eV, 36.8 eV and 530.3 eV are assigned to W 4f_{7/2}, W 4f_{5/2} and O 1s of WFe0, respectively, indicating that the tungsten and oxygen in the h-WO₃ nanostructure exist as W⁶⁺ and O²⁻ [28]. However, these data exhibit a positive shift in WFe0.10 due to the fact that the electrons transfer from WO₃ to Fe species, which leads to the binding energy of W and O increase at last, so FeWO₄ and Fe₂O₃ can separate the photoelectrons [16,25]. In addition, according to the shape change of W spectrum of WFe0.10, we speculate that there is another strong interaction existing between Fe and W except overall shift of the electron. To identify the speculation, we have made peak separation for W and Fe of WFe0.10. As shown in Fig. 5c, the binding energy values of W4f show doublet for W⁵⁺ (35.1 and 36.7 eV) and W⁶⁺ (35.5 and 37.8 eV) [29], indicating that some W⁶⁺ are reduced to W⁵⁺ after introduction of the Fe³⁺ cations and this is consistent with the infrared spectra (Fig. 2). The Fig. 5d presents the Fe 2p_{3/2} and 2p_{1/2} binding energy, where deconvolution yields two pairs of peaks for Fe²⁺ (710.5 and 723.3 eV) and Fe³⁺ (712.8 and 726.1 eV), with a satellite peak at 717.8 eV [30,31]. Understandably, most of Fe²⁺ comes from the FeWO₄ and trace may be from the reduced Fe³⁺ while the Fe³⁺ comes from Fe₂O₃, and the atomic ratio of Fe²⁺/Fe³⁺ is close to 1 which is calculated from their respective areas in the Fe binding energy spectrum, and the mole ratio of FeWO₄/Fe₂O₃ is 2. So the amount of FeWO₄ and Fe₂O₃ can be calculated and presented in Table 1. From the above analysis, there is a truly complex electronic interaction between W and Fe though the content of Fe is rare (Fe 2.62 at.%, in the XPS detection) in WFe0.10, and this might be the reason why FeWO₄ and Fe₂O₃ can highly and firmly disperse on the WO₃ surface.

The band gap energy (E_g) is one of the most important characteristics of a semiconductor material and Tauc plot can be applied to calculate E_g via extrapolation intercept method, $(F(R_\infty)h\nu)^m$ versus incident photon energy ($h\nu$). In which, $F(R_\infty)$, h and ν are absorption coefficient, Planck constant and light frequency, respectively. $F(R_\infty)$ is converted from the UV-vis diffuse reflection absorption spectrum by the Kubelka–Munk function:

$$F(R_\infty) = (1 - R_\infty)^2 / (2R_\infty)$$

Where, R_∞ is relative diffuse reflectance and it has following relationship with reference material:

$$R_\infty = R'_\infty(\text{Material}) / R'_\infty(\text{Reference})$$

$$A = \log(1/R'_\infty(\text{Material}))$$

In which, R'_∞ is absolute diffuse reflectance, BaSO₄ is commonly used as reference sample and its R'_∞ is about 1, thus $R_\infty = R'_\infty(\text{Material})$ and A is the diffuse reflection absorbance. In particular, it is considered one semiconductor has an indirect band gap when its E_g value is less than 3.0 eV [32] and $m = 1/2$ for indirect band gap. Fig. 6a shows the UV-vis diffuse reflection absorption spectra of all WFe_x and it can be observed that all samples show strong absorption in visible region due to their own optical properties. In addition, obvious red shifts and absorption enhancements happen in all di-modified WFe_x samples and they are reinforced by gradually increasing the Fe content. There is no doubt that the introduction of Fe³⁺ cations can make above changes in UV-vis spectrum because the FeWO₄ and Fe₂O₃ have visible light activity and lead to extra absorptions and red shifts, accordingly, the more Fe₂O₃ and FeWO₄ form, the more obvious red-shifts have. The corresponding optical images of all WFe_x are also placed in Fig. 6a, and plainly the color deepens gradually with Fe content rising. Herein, the E_g is extracted for all WFe_x by plotting $(F(R)h\nu)^{1/2}$ vs $h\nu$ as shown in Fig. 6b. For unmodified WFe0, the E_g is 2.79 eV and the E_g of WFe0.07, WFe0.10 and WFe0.20 are 2.68, 2.62 and 2.31 eV, respectively. So, the introduction of FeWO₄ and Fe₂O₃ can significantly reduce the E_g and increase the visible light absorption.

3.2. Photocatalytic activity for degradation of organic dyes

The initial photocatalytic activities of all WFe_x samples were evaluated by the degradation of MB under visible light irradiation ($\lambda > 420$ nm). The Fig. 7a (Fig. S4) shows the time profiles of MB degradation over all WFe_x and H₂O₂, and the activity of H₂O₂ is extremely low. However, in the presence of little H₂O₂, the photoreaction

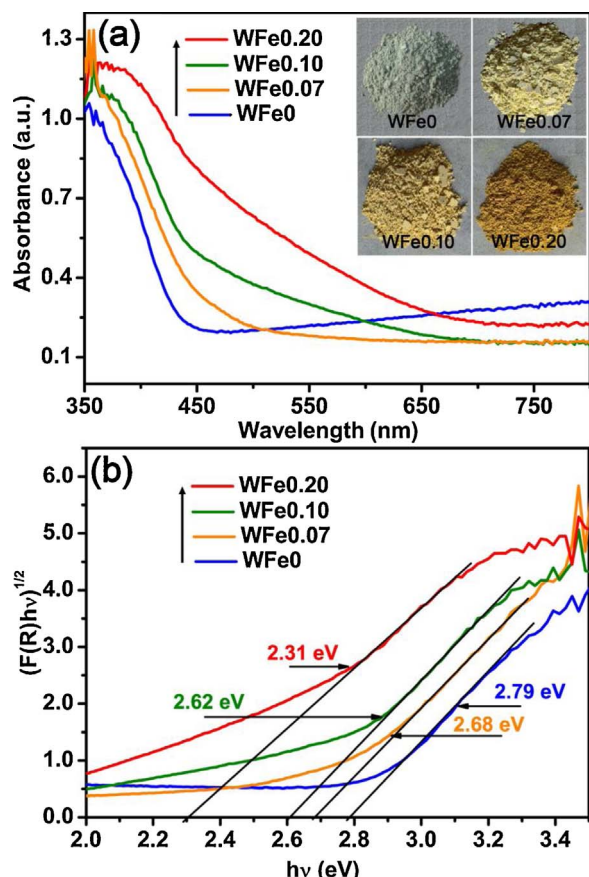


Fig. 6. (a) UV-vis diffuse reflection absorption spectra of all WFe_x samples; (b) the Tauc plots, $(F(R_{\infty})h\nu)^m$ versus $h\nu$, $m = 1/2$ for the indirect band gap of the WO₃ and WO₃·0.33H₂O.

of all WFe_x materials become fast. The degradation ability of WFe0.07 is similar to unmodified WFe0 and both of them have equal efficiency η of 95% after 60 min. What makes us feel excited is that the reaction of WFe0.20 is super fast and obtains η of 95% in such short time of 10 min, so the contribution of H₂O₂ in degradation can be ignored in this period. In order to get intuitive photocatalytic reactivity quantitatively, it is necessary to calculate the apparent rate constant k of catalysts. As we all know, when the concentration of organic dye is low and the process of photodegradation accords with a pseudo-first-order kinetics equation: $-\ln(C/C_0) = kt$, where, C is the concentration at any time (t), C_0 is the initial concentration, k is the apparent reaction rate constant and t is the reaction time. The slope obtained the linear plot of $-\ln(C/C_0)$ (or $\ln(C_0/C)$) with t gives the k value in min^{-1} . So the corresponding kinetic plots and k values are given in Fig. 7b & Table 1, the k value increases with the Fe content and WFe0.20 get the maximum k value of $29.87 \times 10^{-2} \text{ min}^{-1}$, which is 5.3 times larger than $5.62 \times 10^{-2} \text{ min}^{-1}$ of WFe0. Because of the introduction of Fe cations, it is hard to say whether the morphologies of di-modified WFe_x samples have a beneficial or detrimental effect on their performance, but the same hexagonal prisms shape occupies the dominant position in these samples, so we speculate that the influence of morphology on the performance can be reduced to a minimum, especially in such a short degradation time. Furthermore, various other catalysts, including commercial WO₃(c-WO₃), Fe₂O₃, FeWO₄ and P25 (TiO₂), are also applied to degrade MB and results are showed in Fig. 7c, d & Table 1. The photoreaction rates of these catalysts are very slow and among them, the FeWO₄ and P25 have the equal k while Fe₂O₃ owns the least k , but WFe0.20 exhibits excellent degradation performance, indicating that Fe plays a quite important role in the FeWO₄/Fe₂O₃ di-modified WO₃ catalysts. Furthermore, the photodegradation of corresponding mechanical mixing samples (Fig. S5) were tested to observe the reaction activity in which WO₃ was separated from the two Fe species. The results show that the introduction of Fe₂O₃ and FeWO₄ individually or simultaneously all reduce the degradation activity of WO₃, and the poor η may be caused by poor contact between WO₃ and FeWO₄ or Fe₂O₃, leading photoexcited electrons of WO₃ are not separated effectively. But in contrast, the WFe0.20 with the same ratio of three materials has high activity, indicating that the FeWO₄/Fe₂O₃ di-modified WO₃ obtained in

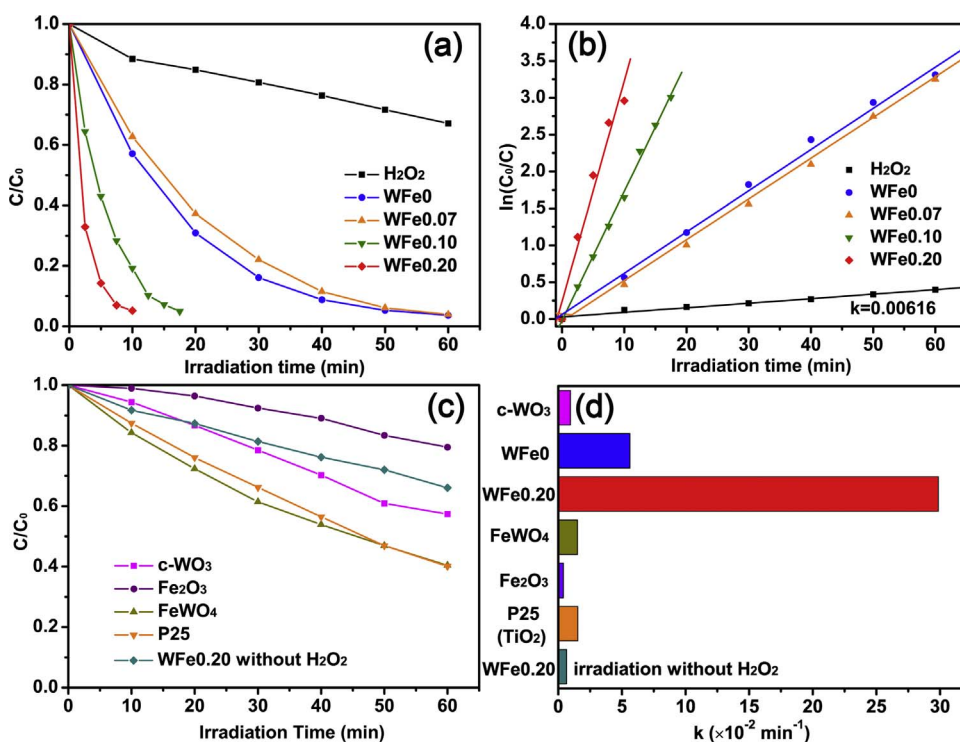


Fig. 7. (a) Photodegradation process over all WFe_x toward MB under visible light irradiation and (b) is the corresponding kinetic analysis through using first-order kinetic model; (c) Photodegradation process over different catalysts; (d) The comparison of first-order rate constant k of MB photodegradation over different catalysts.

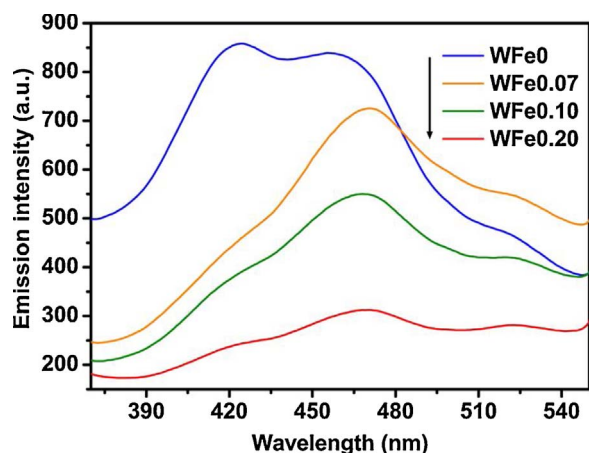


Fig. 8. Photoluminescence spectra of all WFe_x samples and solids were excited at 300 nm.

our work have special coupling structure and higher activity in degradation MB. Moreover, we also tested the photodegradation ability of WFe0.20 in an aerated aqueous without H₂O₂ (Fig. S6), predictably, the reaction is so slow that the k value is only $0.62 \times 10^{-2} \text{ min}^{-1}$, being same as blank experiment of H₂O₂, in other words, there is almost no activity over WFe0.20 when the H₂O₂ is absent. Therefore, the coexistence of FeWO₄, Fe₂O₃ and H₂O₂ is the determinate factor in improving photocatalytic performance of WO₃. Because the FeWO₄ and Fe₂O₃ clusters (or small nanoparticles) on WO₃ surface could act as electron traps, so the photoexcited electrons of WO₃ can be captured, then consumed by a valence decrease of Fe³⁺ → Fe²⁺. Subsequently, the Fenton reaction between Fe²⁺ and H₂O₂ happens and generates ·OH to react with organic dye. In this process, the Fe²⁺ is oxidized to Fe³⁺ again, and then the cycle continues. Of course, Fenton reaction begins directly on FeWO₄.

In order to certify the FeWO₄/Fe₂O₃ di-modified WO₃ catalysts have

the ability of separation photoelectrons, the photoluminescence spectrum (PL) is used in our work. As shown in Fig. 8, the PL spectra of all WFe_x with an excitation wavelength of 300 nm display three emission peaks near the 420, 467 and 520 nm, respectively. According to the literatures, the strong blue emissions at 420 and 467 nm may originate from surface oxygen defects and recombination of electron/hole pairs excited on the surface of material [33,34] while the visible emission around 520 nm is ascribed to the localized state in the band gap [34,35]. The intensity of emission peaks indicates that WFe0 has lots of oxygen vacancies and the highest recombination rate of electron/hole. Obviously, the introduction of Fe³⁺ cations can modify WO₃ surface, reduce surface defects and enhance the charge separation greatly, and efficiency of the charge separation increases with the Fe content. Meanwhile the reduction of visible emission around 520 nm is slower than other peaks, this may be caused by self-excitation of Fe₂O₃ and FeWO₄ at same position. In conclusion, the introduction of Fe³⁺ cations can significantly reduce the recombination of photoexcited electrons and holes of WO₃, which offers the possibility of efficient photocatalytic degradation.

Considering all WFe_x have different specific surface areas, to further compare the real photocatalytic efficiency over unit area of the catalysts, the determined apparent reaction rate constant k is normalized to the specific surface areas, referred to as k_s given in Table 1. The k_s values of WFe0.07, WFe0.10 and WFe0.20 are 5.00×10^{-2} , 3.64×10^{-2} and $2.21 \times 10^{-2} \text{ min}^{-1} \text{ m}^{-2} \text{ g}$, respectively, and the rule of these k_s values is opposite to corresponding k values. The WFe0.07 and WFe0.10 have larger k_s in comparison with other WFe_x, and this improvement could be attributed to the two following reasons: (1) Trace amount of Fe species promotes the separation and consumption of electrons rapidly; (2) According to the literatures [36–39], bicrystalline materials can enhance the photocatalytic activity effectively, and we think biphasic substrate WO₃ in this work may also have some contributions to its high activity. For WFe0.20, the smaller k_s may be caused by agglomeration of Fe species and resulting surface adsorption difference in sample. However, for the photocatalytic reaction, the

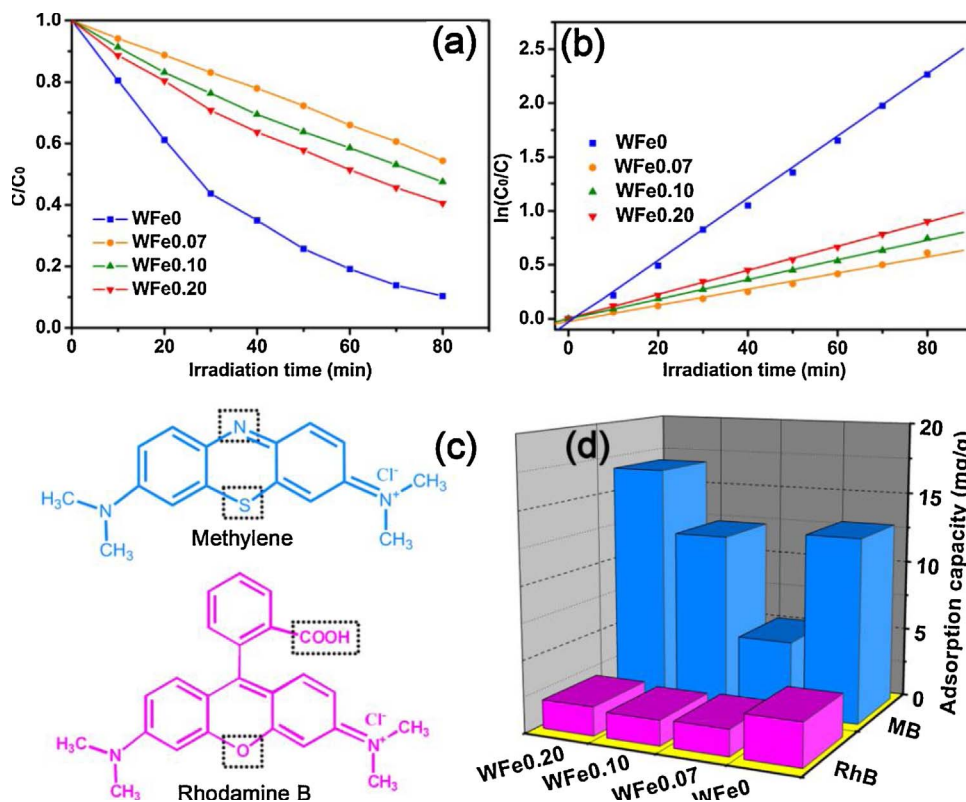


Fig. 9. (a) Photodegradation process over all WFe_x toward RhB under visible light irradiation and (b) is the corresponding kinetic analysis through using first-order kinetic model; (c) The molecular structure of MB and RhB dyes; (d) The adsorption capacity of MB and RhB dyes on all WFe_x.

specific surface of catalyst is a very important factor and directly influences adsorption in the first step of the degradation reaction. Therefore, the WFe0.20 with the BET of $13.51 \text{ m}^2 \text{ g}^{-1}$ has excellent photocatalytic activity in degradation MB, although it has a relatively small k_s value of $2.21 \times 10^{-2} \text{ min}^{-1} \text{ m}^{-2} \text{ g}$.

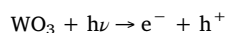
As a distinguished catalyst, it is always hoped to have high activity in degradation of different dyes, then we also evaluated the ability of all WFe x in the degradation of RhB and the results are showed in Fig. 9 a, b & S7. Unfortunately, the k values of di-modified WFe x are all less than unmodified WFe0, even the best WFe0.20, its k value is only $1.11 \times 10^{-2} \text{ min}^{-1}$ and much smaller than that of WFe0 ($k = 2.89 \times 10^{-2} \text{ min}^{-1}$). What makes this difference? The answer is given in here. All WFe x have different adsorption capacity toward MB and RhB dyes due to intrinsic difference in molecular structures of dyes (Fig. 9c). Comparing the two dyes, the steric hindrance may hinder adsorption but the main reason we speculated is that the MB dye molecular contains weak electronegative N and S, which acts as electron-donating group and is prone to inject electrons to empty d orbital of metal element, while the O in RhB cannot play similar role. Thus, the adsorption of MB on all WFe x is stronger than RhB as shown in Fig. 9d and the adsorption capacity increases with the specific surface area except for WFe0. In addition, adsorption increments (Fig. S8) per unit area of WFe0.07, WFe0.10 and WFe0.20 are 3.08, 2.19 and $1.10 \text{ mg g}^{-1} \text{ m}^{-2}$, respectively, they are all larger than WFe0 ($0.53 \text{ mg g}^{-1} \text{ m}^{-2}$). Undoubtedly, it is a fact that introduction of little Fe^{3+} cations can significantly increase the adsorption capacity of MB and this is because that there is a stronger relationship of donation and reception electrons between N, S and Fe element, especially N [40,41], and it provides a prerequisite for rapid degradation of MB dye. Furthermore, the results of adsorption increments are corresponding with their k_s toward degradation of MB. As we all know, agglomeration will inevitably appear with the increase Fe content, so weak peaks of FeWO_4 and Fe_2O_3 appear in XRD spectrum of WFe0.20, meaning Fe species turns into small nanoparticles (WFe0.20) from clusters (WFe0.07) and then decreases the adsorption capacity of WFe0.20 over unit area.

In order to illustrate the contribution of N, S in the dyes, three important dyes of Toluidine blue (TB), AzureI(AI) and Acridine orange (AO) that possess similar quasi-phenothiazine structures were carried out degradation experiments over WFe0.20 and WFe0, respectively, and the results are presented in Fig. 10 a–f & S9. For WFe0, the degradation η achieves of 90%, 91% and 90% in 40, 20 and 30 min for TB, AI and AO, respectively, and the reaction rate of WFe0.20 is so fast that it obtains same η within 12.5, 7.5 and 5 min. The k values reach 25.71×10^{-2} , 45.03×10^{-2} and $48.67 \times 10^{-2} \text{ min}^{-1}$ in line area for the three dyes, and they are about 4.4, 3.8 and 5.8 times larger than WFe0, respectively. As expected, the adsorption capacities of WFe0.20 are all larger than WFe0 toward TB, AI and AO dyes (Fig. S10). Thus, the above results indicate that the di-modified WFe0.20 catalyst has a perfect degradation effect on quasi-phenothiazine dyes. Moreover, the third-recycled WFe0.20 still exhibited good photocatalytic activity (Fig. S11) in the stability test, showing that the di-modified WFe x was photostable.

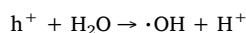
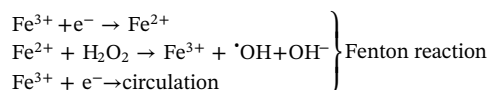
Based on the experimental results, the di-modified WFe x catalysts have super photocatalytic activity in degradation of quasi-phenothiazine dyes and it is necessary to explore reaction mechanism of such catalyst. The conduction band (CB) potential of WO_3 is 0.2–0.8 eV and theoretical prediction from the absolute Mulliken electronegativity is a reasonable strategy to determine the potential levels of oxide semiconductor [9]. The CB edge of a semiconductor can be calculated by the following equation: $E_{(\text{cb})} = X - E_c - 0.5E_g$, where, X is geometric mean of the Mulliken's electronegativity of constituent atoms; E_c is the energy of free electrons on the hydrogen scale (ca. 4.5 eV) and E_g is the band gap of the semiconductor. We have measured E_g of 2.79 eV for WFe0 in DRS spectrum, the calculated CB and VB positions of WFe0 are $+0.69 V_{\text{NHE}}$ and $+3.48 V_{\text{NHE}}$, respectively (The specific calculation process is placed in Table S1). In addition, according to the literatures

[14,18–21], CB of FeWO_4 and Fe_2O_3 clusters (or small nanoparticles) are 0.55–0.73 eV and 0.46–0.77 eV, respectively and it is possible that the photoinduced electrons would transfer from CB of WO_3 to that of FeWO_4 and Fe_2O_3 , leaving the corresponding photogenerated holes in the valence band (VB) when the di-modified WO_3 is irradiated by visible light. It is also reported that the electrons will be captured by the low energy trapping sites of Fe_2O_3 when its CB is even higher than WO_3 [16]. So as long as the energy matches, no matter what the CB of Fe species is, little higher or lower than the WO_3 , the electrons will migrate to the Fe species, then Fe^{3+} is reduced to Fe^{2+} , followed by Fenton reaction with H_2O_2 to generate $\cdot\text{OH}$ radicals and Fe^{3+} , meanwhile, the holes left in the VB of WO_3 also produce the $\cdot\text{OH}$ radicals. The typical process just as shown in Fig. 11, all $\cdot\text{OH}$ radicals react with dyes while Fe^{3+} accepts photoexcited electron to begin new cycle. It is worth mentioning that the FeWO_4 and Fe_2O_3 on WO_3 surface also can be excited to produce electrons and holes, but they make less contribution to total degradation efficiency under visible light irradiation (Fig. 7c and d).

The above important process of photocatalytic degradation is concluded as following:



$e^- \rightarrow$ Migrate to the CB of FeWO_4 and Fe_2O_3 clusters (or small nanoparticles)



4. Conclusion

In summary, as an effective photocatalyst for degradation of organic dyes under visible light, the $\text{FeWO}_4/\text{Fe}_2\text{O}_3$ di-modified WO_3 was successfully designed and prepared using a facile one-step hydrothermal method. The FeWO_4 and Fe_2O_3 clusters (or small nanoparticles) formed during the experiment firmly and highly disperse on the WO_3 surface, and they can effectively accelerate the photocatalytic activity of WO_3 due to the fact that both of them can separate and consume photoexcited electrons by matching CB with WO_3 and Fenton reaction in the presence of trace H_2O_2 . Furthermore, it is found that the di-modified WO_3 samples exhibit good selective adsorption toward quasi-phenothiazine dyes because of the interaction between weak electronegative element of N, S and Fe. The WFe0.20, which has the highest BET, displays super high photocatalytic activity in degrading quasi-phenothiazine dyes of MB, TB, AI and AO, and the corresponding k values are 5.3, 4.4, 3.8 and 5.8 times larger than pure WO_3 , respectively. In addition, the synthetic method presented in this work accords with the requirements of today's environmental protecting, energy saving and efficient economy.

Acknowledgements

This work was supported by the National Natural Science Foundation of China (No. 21373010), Youth Innovation Promotion Association CAS (No. 2015141 and 2016377), Excellent Youth Scholars of State Key Laboratory of Coal Conversion (No. 2016BWZ001), Shanxi Province Science Foundation for Youths (201701D211005) and Synfuels China Technology Company Limited.

Appendix A. Supplementary data

Supplementary data associated with this article can be found, in the

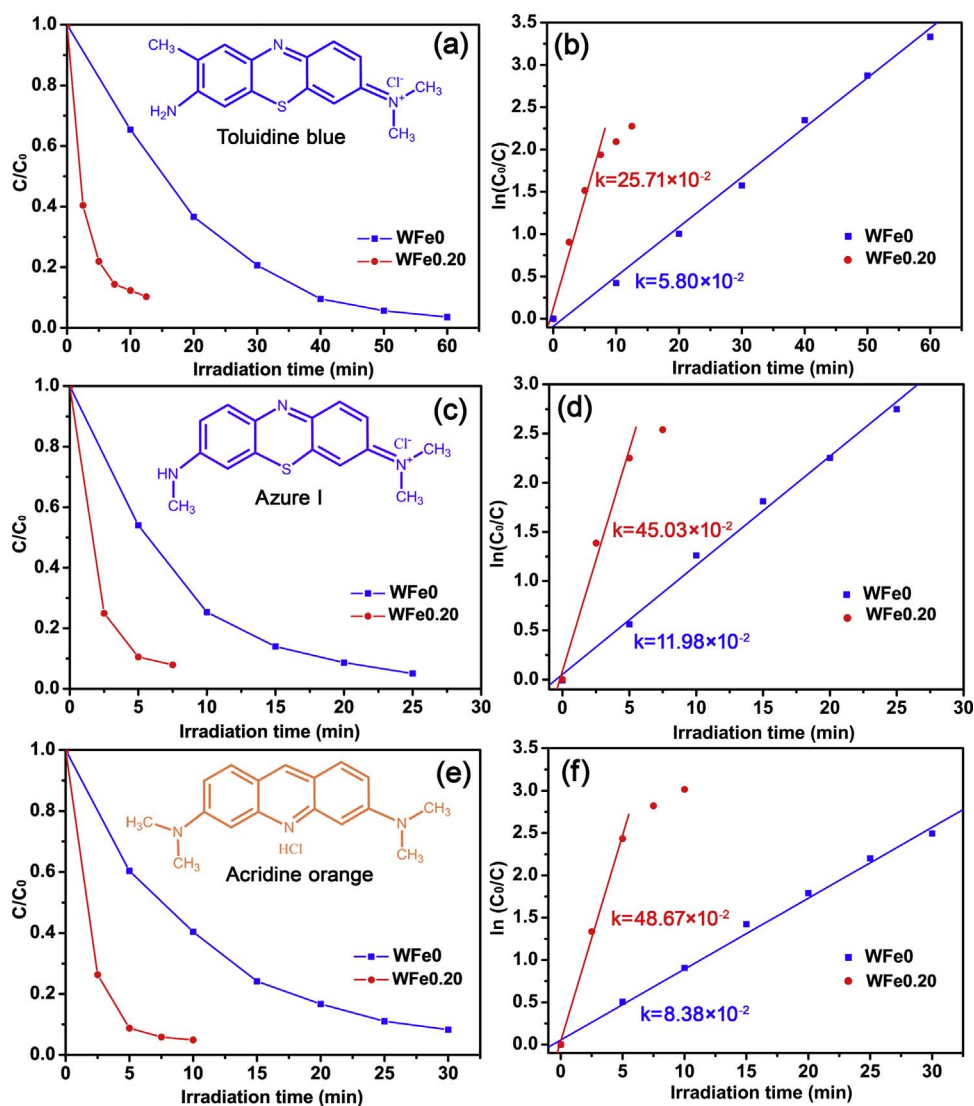


Fig. 10. (a,c,e) Photodegradation process over WFe0.20 and WFe0 toward TB, AI and AO dyes under visible light irradiation and (b,d,f) is the corresponding kinetic analysis through using first-order kinetic model.

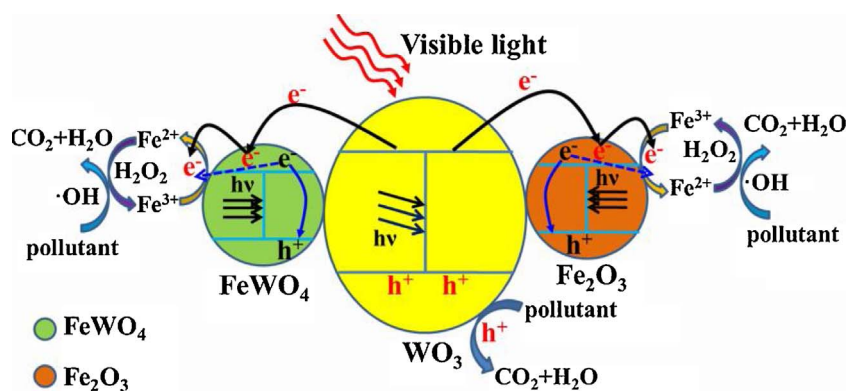


Fig. 11. Proposed mechanism of photocatalytic degradation of organic dyes by $\text{FeWO}_4/\text{Fe}_2\text{O}_3$ di-modified WO_3 catalyst under visible light irradiation.

online version, at <http://dx.doi.org/10.1016/j.apcatb.2017.09.011>

References

- [1] H. Tong, S. Ouyang, Y. Bi, N. Umezawa, M. Oshikiri, J. Ye, *Adv. Mater.* 24 (2012) 229–251.
- [2] M. Mrowetz, W. Balcerski, A.J. Colussi, M.R. Hoffmann, *J. Phys. Chem. B* 108 (2004) 17269–17273.
- [3] R. Shi, J. Lin, Y. Wang, J. Xu, Y. Zhu, *J. Phys. Chem. C* 114 (2010) 6472–6477.
- [4] M.T. Nenadovic, T. Rajh, O.I. Micic, *J. Phys. Chem.* 88 (1984) 5827–5830.
- [5] E. Endoh, J.K. Leland, A.J. Bard, *J. Phys. Chem.* 90 (1986) 6223–6226.
- [6] J. Kim, C.W. Lee, W. Choi, *Environ. Sci. Technol.* 44 (2010) 6849–6854.
- [7] H. Widiyandari, A. Purwanto, R. Balgis, T. Ogi, K. Okuyama, *Chem. Eng. J.* 180 (2012) 323–329.
- [8] Y. Miseki, H. Kusama, H. Sugihara, K. Sayama, *J. Phys. Chem. Lett.* 1 (2010) 1196–1200.
- [9] H. Wang, G. Zhang, Y. Xu, X. Wei, X. Shen, Y. Sun, *CrystEngComm* 18 (2016) 8089–8100.
- [10] M. Amini, B. Pourbadiei, T.P.A. Ruberu, L.K. Woo, *New J. Chem.* 38 (2014) 1250–1255.
- [11] R. Abe, H. Takami, N. Murakami, B. Ohtani, *J. Am. Chem. Soc.* 130 (2008) 7780–7781.
- [12] S. Sun, W. Wang, S. Zeng, M. Shang, L. Zhang, *J. Hazard. Mater.* 178 (2010) 178–180.

- 427–433.
- [13] Z.G. Zhao, M. Miyauchi, *Angew. Chem.* 120 (2008) 7159–7163.
- [14] D. Bi, Y. Xu, *Langmuir* 27 (2011) 9359–9366.
- [15] H. Irie, S. Miura, K. Kamiya, K. Hashimoto, *Chem. Phys. Lett.* 457 (2008) 202–205.
- [16] D. Bi, Y. Xu, *J. Mol. Catal. A* 367 (2013) 103–107.
- [17] M. Mishra, D. Chun, *Appl. Catal. A* 498 (2015) 126–141.
- [18] G. He, M. Chen, Y. Liu, X. Li, Y. Liu, Y. Xu, *Appl. Surf. Sci.* 351 (2015) 474–479.
- [19] S. Bera, S.B. Rawal, H.J. Kim, W.I. Lee, *ACS Appl. Mater. Interfaces* 6 (2014) 9654–9663.
- [20] X. Cao, Y. Chen, S. Jiao, Z. Fang, M. Xu, X. Liu, L. Li, G. Pang, S. Feng, *Nanoscale* 6 (2014) 12366–12370.
- [21] Y. Ma, Y. Guo, H. Jiang, D. Qu, J. Liu, W. Kang, Y. Yi, W. Zhang, J. Shi, Z. Han, *New J. Chem.* 39 (2015) 5612–5620.
- [22] Z. Wang, S. Zhou, L. Wu, *Adv. Funct. Mater.* 17 (2007) 1790–1794.
- [23] M. Gotic, M. Ivanda, S. Popovic, S. Music, *Mater. Sci. Eng. B* 77 (2000) 193–201.
- [24] M.F. Daniel, B. Desbat, J.C. Lassegues, *J. Solid State Chem.* 67 (1987) 235–247.
- [25] K. Buvaneswari, R. Karthiga, B. Kavitha, M. Rajarajan, A. Suganthi, *Appl. Surf. Sci.* 356 (2015) 333–340.
- [26] S. Zhan, D. Chen, X. Jiao, S. Liu, *J. Colloid Interface sci.* 308 (2007) 265–270.
- [27] J. Pfeifer, C. Guifang, P. Tekula-Buxbaum, B.A. Kiss, M. Farkas-Jahnke, K. Vadasdi, *J. Solid State Chem.* 119 (1995) 90–97.
- [28] H. Xia, Y. Wang, F. Kong, S. Wang, B. Zhu, X. Guo, J. Zhang, Y. Wang, S. Wu, *Sens. Actuators B* 134 (2008) 133–139.
- [29] N. Xu, M. Sun, Y.W. Cao, J.N. Yao, E.G. Wang, *Appl. Surf. Sci.* 157 (2000) 81–84.
- [30] L. Lin, Q. Zhu, A.W. Xu, *J. Am. Chem. Soc.* 136 (2014) 11027–11033.
- [31] W. Niu, L. Li, X. Liu, N. Wang, J. Liu, W. Zhou, Z. Tang, S. Chen, *J. Am. Chem. Soc.* 137 (2015) 5555–5562.
- [32] J.Y. Zheng, G. Song, J. Hong, T.K. Van, A.U. Pawar, D.Y. Kim, C.W. Kim, Z. Haider, Y.S. Kang, *Cryst. Growth Des.* 14 (2014) 6057–6066.
- [33] C. Su, H. Lin, *J. Phys. Chem. C* 113 (2009) 4042–4046.
- [34] J. Ha, P. Muralidharan, D.K. Kim, *J. Alloys Compd.* 475 (2009) 446–451.
- [35] C. Paracchini, G. Schianchi, *Phys. Status Sol. A* 72 (1982) K129–K132.
- [36] J. Zhang, Q. Xu, Z. Feng, M. Li, C. Li, *Angew. Chem. Int. Ed.* 47 (2008) 1766–1769.
- [37] G. Liu, Z. Chen, C. Dong, Y. Zhao, F. Li, G.Q. Lu, H. Cheng, *J. Phys. Chem. B* 110 (2006) 20823–20828.
- [38] W. Li, C. Liu, Y. Zhou, Y. Bai, X. Feng, Z. Yang, L. Lu, X. Lu, K. Chan, *J. Phys. Chem. C* 112 (2008) 20539–20545.
- [39] Y. Li, Z. Tang, J. Zhang, Z. Zhang, *Appl. Catal. B* 207 (2017) 207–217.
- [40] F. He, X. Deng, M. Chen, *Chemosphere* 168 (2017) 623–629.
- [41] Z. Liu, B. Lv, D. Wu, Y. Sun, *Particuology* 10 (2012) 456–461.